**Efficient Se-rich $Sb_2Se_3$/CdS planar-heterojunction solar cells by sequential processing: control and influence of Se content**

*Pedro Vidal-Fuentes, Marcel Placidi, Yudania Sánchez, Ignacio Becerril Romero, Jacob Andrade-Arvizu, Zacharie Jehl, Alejandro Pérez-Rodríguez, Víctor Izquierdo-Roca, and Edgardo Saucedo*

P. Vidal-Fuentes (e-mail: pvidal@irec.cat), Dr. M. Placidi, Dr. Y. Sánchez, Dr. I. Becerril-Romero, J. Andrade-Arvizu, Dr. Z. Jehl, Prof. Dr. A. Pérez-Rodríguez, Dr V. Izquierdo-Roca, Dr E. Saucedo (e-mail: esaucedo@irec.cat).

Catalonian Institute for Energy Research (IREC), Jardin de les Dones de Negre 1, 08930 Sant Adrià de Besòs, Barcelona, Spain.

Prof. Dr. A. Pérez-Rodríguez

IN2UB, Departament d'Enginyeria Electrònica i Biomèdica, Universitat de Barcelona, c. Martí i Franquès 1, 08028 Barcelona, Spain

Keywords: thin film solar cells, quasi one-dimensional materials, $Sb_2Se_3$, sequential process

## Abstract

Quasi-one-dimensional chalcogenides are under the spotlight due to their unique properties for several technological applications including computing, photonic, sensing and energy conversion. In particular, antimony chalcogenides have recently experienced incredible progresses as emerging photovoltaic materials. In this work, the fabrication by a sequential process of $Sb_2Se_3$ solar cells is addressed, and the annealing temperature is found as the main parameter controlling the composition of the Se-rich absorbers. Building on this, a systematic study of the evolution of the optolectronic parameters of the solar cells as a function of the Se excess is presented together with a thourough characterization of the devices that sheds light on their main limiting factors. A record power conversion efficiency of 5.7% is achieved, the highest reported value using reactive annealing on a metallic precursor for this material.

## 1. Introduction

Thin film photovoltaic (TFPV) chalcogenide absorbers such as cadmium telluride (CdTe) and $Cu(In,Ga)(S,Se)_2$ (CIGS) are reaching maturity with record power conversion efficiencies (PCE) of 22.1 % and 23.35 % respectively, leading to an increase in their industrial deployment and module production.[1,2] While these technologies are achieving remarkable results among TFPV materials approaching values of those of Silicon solar cells, they contain elements that are considered either scarce (like In and Ga in CIGS, or Te in CdTe) or toxic (like Cd in CdTe), which will hamper their deployment beyond the Terawatt level.[3,4] The past 10 years have seen the emergence of new chalcogenide materials for TFPV applications which, while inspired by CdTe and CIGS, alleviate the material scarcity issue by being based on abundant elements. While important progresses were made in that regard, the large complexity of the most successful Earth-abundant chalcogenide compounds, Cu2SnZn(S,Se)4 (CZTSSe or kesterite) has led to stalling performances that remain below 13 %,[5] resulting in a declining interest from the industry. In that context, returning towards simpler compounds with less than 4 elements presents an attractive path for the development of further TFPV technologies. Several of these simpler materials have recently attracted a lot of interest, such as the binary compounds SnS, GeSe and $Sb_2(S,Se)_3$, the ternary compounds $CuSb(S,Se)_2$, and $Cu_2Sn(S,Se)_3$, and even elemental Se.[3,6–18]

Among them, quasi one-dimensional (Q-1D) antimony chalcogenide compounds have demonstrated a promising performance increase within a short timeframe (see **Table 1**), with a very recent record of 9.2 % PCE reported for a $Sb_2Se_3$ device in a non-planar configuration.[18] Additionally, Q-1D $Sb_2Se_3$ is formed by earth-abundant and low toxicity constituents, and has shown various properties that position it as a strong candidate for low cost TFPV applications: its single stable phase (similarly to CdTe, hence avoiding issues with secondary phase formation), an almost optimal bandgap (1.0-1.20 eV indirect and 1.17-1.30 eV direct ), a large absorption coefficient above the bandgap (around

$10^5$ $cm^{-1}$) and a carrier lifetime of 67 ns, higher than that of kesterite and most chalcopyrite materials.[19]

An important characteristic of this material is its Q-1D crystal structure forming ribbons stacked by van der Waals forces that confer it anisotropic conduction properties, and in principle benign grain boundaries (absence of dangling bonds) possibly leading to preferential carrier transport along the ribbons and low recombination losses in solar cell devices.[15,20] Moreover, recent works have demonstrated the possibility of controlling the orientation during the $Sb_2Se_3$ growth by choosing an adequate substrate, a crucial step for high performance.[21,22] However, little is known about the influence of the film composition on the photovoltaic response of the $Sb_2Se_3$ devices, and previous studies on CIGS and CZTS have demonstrated how critical it can be in controlling the presence of defects within the layer. [23,24] Typically, the best $Sb_2Se_3$ reported solar cells are achieved under Se-rich conditions which tends to reduce the presence of Se vacancies ($V_{Se}$) and substitutional defects (especially $Sb_{Se}$) acting as donor impurities. Se vacancies have been widely reported as the main recombination centers and ascribed to performance degradation, especially in thermally evaporated devices.[25] Nevertheless, post-deposition steps such as selenization have been reported to be highly effective in reducing the density of Se vacancies.[26]

It can be seen in Table 1 that most of the record devices are fabricated through evaporation or closed space sublimation, and in superstrate configuration.[18,21,27–45] Very few groups have been focusing on a substrate configuration, and only one study reported a sequential route based on the selenization of a sputtered Sb precursor which resulted in a very low PCE (0.72 %).[46] In this work, we aim at extending the $Sb_2Se_3$ technology towards substrate configuration and sequential processing, which is of high importance for future development of cost-effective applications based on this technology.

As such, a sequential route based on the selenization of thermally evaporated Sb layers is proposed. This work is divided in two main parts. First, a broad analysis is conducted and the most relevant process parameters that lead to good quality Se-rich $Sb_2Se_3$ PV absorbers with an adequate orientation and no secondary phases are identified. The composition of the layers is shown to be controllable

through the temperature of the reactive annealing, demonstrating the optimal elemental ratio and leading to the fabrication of a Glass/Mo/$Sb_2Se_3$/CdS/i-ZnO/ITO based solar cell with a 5.7 % PCE, the highest reported value for an absorber synthesized by a sequential process in substrate configuration. The second part of the work focuses, on a deep analysis of the optoelectronic properties of the best device. From this results, the main PCE limitations of the $Sb_2Se_3$ absorber are identified, and strategies for further improvement of the device architecture are proposed.

## 2. Results and discussion

### 2.1. Synthesis of $Sb_2Se_3$ absorbers by a sequential process: how to control the 3[Sb]/2[Se] ratio.

$Sb_2Se_3$ thin film solar cells were fabricated in substrate configuration (in contrast to most of the works reported with this material, as shown in Table 1) by a sequential process, as described in the experimental section (see Supporting Information **Figure S1**). The annealing atmosphere was controlled by fixing the amount of Se powder (25 mg) and by varying several other parameters such as temperature, pressure and time. Due to the lack of information about $Sb_2Se_3$ processing through reactive annealing of a Sb layer, the first part of the work is focused on understanding the influence of the different annealing parameters on relevant structural properties of this Q-1D material.

The influence of reactive annealing temperature on the composition of the $Sb_2Se_3$ layer was first investigated by varying it from 300 ºC up to 400 ºC while fixing the rest of the parameters. This way, the heating ramp was fixed to 20 ºC $min^{-1}$, the processing time to 30 min and the pressure to 500 mbar. **Figure 1a** shows the change in composition in the range of temperatures investigated determined by X-ray fluorescence (XRF) measurements. The results show that the layers are consistently Se-rich (3[Sb]/2[Se] < 1) and, interestingly, the 3[Sb]/2[Se] ratio is found to decrease with the increasing annealing temperature. This is an important result since it implies that it is possible to adjust the absorber composition within a wide range in a simple way by varying the annealing temperature. Despite the observed Se excess, X-ray diffraction (XRD) and Raman spectroscopy measurements

(under Se resonant conditions) (Figure 1b and 1c) shows no evidence of elemental Se secondary phases in the samples processed in the 300-380 ºC range. Therefore, it can be assumed that the selenium excess is completely assimilated into the structure of the absorber. In contrast, both elemental Se and α-$Sb_2O_3$ secondary phases are clearly detected in the sample processed at 400 ºC, the peak assignation of the different phases can be found elsewhere. [47] Thus, it seems that such high amount of Se exceeds the assimilation capacity of the lattice and leads to the segregation of elemental Se at the surface of the film.[48,49] On the other hand, the presence of α-$Sb_2O_3$ detected in the samples annealed at 400 ºC is probably arising from the decomposition of $Sb_2Se_3$ and subsequent oxidation of the resulting elemental Sb when exposed to the atmosphere. [50] It can thus be inferred that the optimum annealing temperature range to obtain Se-rich single phase $Sb_2Se_3$ lies within a broad temperature range from 300 ºC to 380 ºC.

XRD measurements were performed on the different samples in order to identify the preferential orientation of the $Sb_2Se_3$ layers (Figure 1c) (only data from 10-50 º is presented for the sake of clarity). Interestingly, no noticeable texture change is observed for annealing temperatures between 300-380 ºC, in agreement with the apparent stability of the process up to this point. A clear preferential [hk1] orientation (JCPDS No. 15– 0861) is observed in all the cases. This orientation is ascribed to vertically aligned ribbons, with negligible presence of undesirable [hk0] planes.[18] Thus, the sequential process developed in this work for the synthesis of $Sb_2Se_3$ layers (and using Glass/Mo as substrate) results in [hk1] oriented ribbons regardless of the annealing temperature. This represents a clear advantage with respect to other fabrication routes. In addition, both Raman and XRD measurements demonstrate that in the $0.78 \leq 3[Sb]/2[Se] \leq 0.92$ composition region, only orthorhombic (Pnmb #62) $Sb_2Se_3$ phase is observed.[47]

Regarding the morphology of the absorbers, cross-sectional scanning electron microscopy (SEM) micrographs on completed devices are shown in Figure 1d. Independently from the annealing temperature, the grains maintain a uniform appearance, without voids or substrate delamination issues, and generally large grains with clear facets forming compact layers. This aligns well with previous

reports on this material.[21] In addition, a clear increase in grain size is observed for annealing temperatures ≥ 350 ºC.

On the other hand, it is also possible to observe the formation of a thin layer in the interface between the Mo and the $Sb_2Se_3$ absorber layer in the samples synthesized at 350 ºC and 380 ºC. This layer, which increase with the annealing temperature form ~75 to ~130 nm, is associated with the formation of a $MoSe_2$ phase which could enhance the contact ohmicity at the back interface, as widely reported for other chalcogenides,[51] and more recently for $Sb_2Se_3$ devices.[21]

The influence of the annealing pressure and duration were also investigated (**Figure 2** and **Figure S2**). Figure S2 shows that at pressures below 500 mbar the obtained $Sb_2Se_3$ absorbers display a degraded absorber morphology with very low homogeneity. This effect could be related to a fast Se evaporation at the beginning of the annealing routine, hindering chalcogen availability during the rest of the process. In contrast, for pressures comprised between 500-1000 mbar, no inhomogeneity is observed. As shown in Figure 2a the highest pressures (500 and 1000 mbar) lead to similar absorber compositions. In addition, the crystalline quality remains unchanged with the increasing annealing pressure as can be deduced from the analysis of the full width at half maximum (FWHM) of the main XRD 211 and 002 reflections (Figure 2c). These results indicate that the suitable pressure range for the synthesis of $Sb_2Se_3$ is broad, between 500 and 1000 mbar, with negligible variations within this range.

Regarding the annealing duration, six different dwell times (from 5 to 60 min) were tested. The annealing temperature was fixed to 320 ºC (this temperature was selected based on the performance of the solar cell devices that will be presented in the next section). No significant changes are observed neither in composition (Figure 2b) nor in the FWHM of the 211 and 002 reflections (Figure 2d) for dwell durations ≤ 30 min. This indicates that for short processing times (up to 30 min), there is almost no Se loss in contrast to what is typically reported in literature employing other deposition techniques, especially with thermal evaporation.[36] However, longer annealing times (60 min), increase the 3[Sb]/2[Se] ratio of the synthesized absorbers close to stoichiometry, suggesting a significant Se loss.

Figure 2e shows cross-sectional SEM images of the samples processed employing different dwell durations. The only noticeable difference between them is a lower grain size for longer processing times, especially for the 60 min annealing. It is interesting to note that large grains and an absence of voids are obtained with annealing durations as short as 5 min.

Thus, from the results shown above, it can be concluded that it is possible to obtain good quality Se-rich $Sb_2Se_3$ layers by reactive annealing of Sb layers. In addition, it has been demonstrated that the annealing temperature can be used to control the composition of the absorber layers while the annealing pressure and duration exhibit a minor influence. In the following section, the impact of the absorber composition on the optoelectronic parameters of the solar cells is investigated.

### 2.2. On the impact of the 3[Sb]/2[Se] ratio on the $Sb_2Se_3$/CdS planar heterojunction properties.

Following the previous results, all the absorbers synthesized at 500 mbar and 1000 mbar were processed into solar cells (using a 30 min dwell time) to investigate on the correlation between the absorber composition and the photovoltaic properties of the completed devices. The results are summarized in **Figure 3** where the most relevant optoelectronic parameters of the single solar cells are plotted as a function of the 3[Sb]/2[Se] ratio of the absorbers including dark and illuminated current density - voltage (J-V), together with capacitance - voltage (C-V) analysis. Observing the evolution of the PCE with the composition (**Figure 3a**), three different regions are clearly distinguished. The main characteristics of each compositional region are now surveyed:

- Region 1: (slightly Se-rich conditions, $0.95 \geq 3[Sb]/2[Se] > 0.90$) All the optoelectronic parameters are below the maximum values obtained in this set of samples with: $V_{oc}$ (around 100 mV, Figure 3b), $J_{sc}$ (around 3 mA $cm^{-2}$, Figure 3c) and FF (around 15% absolute, Figure 3d). Looking at the analysis of dark J-V curves (Figure 3e), it is clear that the samples in this region suffer from a very low shunt resistance ($R_{sh}$),only one order of magnitude higher than series resistance ($R_s$). This correlates with the low $V_{oc}$ and deteriorated FF. Since no pinholes

were observed in these samples, such an unusually low $R_{sh}$ may be arising from direct conduction through unpassivated grain boundaries creating preferential shunt-paths. On the other hand, the series resistance of the devices can be considered low (1.5 $\Omega cm^2$), consistent with the good crystalline quality and the beneficial [001] preferential orientation of the absorbers. Likewise, the apparent carrier concentration estimated from CV measurements is in the $10^{16}$-$10^{17}$ $cm^{-3}$ range, typical for $Sb_2Se_3$ and other chalcogenide devices with good conversion efficiencies.[18,52] However, the results indicate that the space charge region (SCR) width is narrow (around 0.25 μm), suggesting possible collection problems. In summary, the main identified problems for this region of slightly Se-rich composition are a low $R_{sh}$ and a narrow SCR.

- Region 2 (Se-rich conditions, $0.90 \geq 3[Sb]/2[Se] > 0.80$): In this region, the $V_{oc}$ (Figure 3b) and FF (Figure 3d) are remarkably increased while $J_{sc}$ is only slightly enhanced (Figure 3c). This is accompanied by a higher $R_{sh}$ (up to two orders of magnitude) as extracted from the dark J-V curves. Furthermore, the $R_{sh}$ of the devices follows an almost exponential increase with Se content (see Figure 3e). Considering that neither the crystalline quality, nor the orientation of the absorber grains are modified with the increasing Se content and that no secondary Se phases are detected, it seems that Se-excess is accumulated within the structure of $Sb_2Se_3$. In fact, a recent work proposes that $Sb_2Se_3$ can accept high concentrations of defects due to weak van der Waals interactions and the large inter-space between the different $[Sb_4Se_6]_n$ atomic chains of the Q-1D structure.[46] The presence of electrically inactive $Se_i$,[26] or even of wide bandgap crystalline elemental Se could hinder electronic hopping in this region, and drastically reduce the conduction at the grain boundaries which could lie at the origin of the improved $R_{sh}$ observed in this region.
- Region 3 (very Se-rich conditions, $3[Sb]/2[Se] \leq 0.80$): Further increase of the Se content leads to a deterioration of the PCE, due to degraded $J_{sc}$ and FF ($V_{oc}$ is not affected). In this

case, the resistances of the devices present favourable values for solar cell performance and thus seem unrelated to the observed low PCE's. However, important changes are observed from the CV analysis (Figure 3f). In particular, the apparent carrier concentration increases, and the SCR width strongly decreases to values as low as 0.10 µm. The latter observation could lead to a lower collection efficiency and an increased recombination at the SCR which is in good agreement and with the low $J_{sc}$ and FF observed in this region. Therefore, it seems clear that a too high Se content somehow affects the $Sb_2Se_3$/CdS heterojunction modifying the electrical properties of the absorber.

In contrast to the large impact of the composition on the optoelectronic parameters of the solar cell devices, the bandgap of the absorber (both, the indirect and the direct bandgaps) calculated by the derivative method from the external quantum efficiency (EQE) of the devices (see **Figure S3** of the S.I.) is not affected by the 3[Sb]/2[Se] ratio.

In the last part of the paper, a detailed characterization of a high PCE device is presented, to further study the relation between Se content and solar cell performance.

### 2.3. Limiting factors for power conversion efficiency in a high efficiency Sb2Se3/CdS planar heterojunction solar cell

In the previous section, it has been demonstrated that the highest PCE are obtained for absorber compositions in the Se-rich region of the $Sb_2Se_3$ phase diagram (3[Sb]/2[Se] = 0.8-0.9) with the record performance obtained for 3[Sb]/2[Se] = 0.88. This section presents a complete optoelectronic characterization of one of these record devices (5.7 % PCE). Raman spectroscopy measurements (**Figure S4)** and XRD data (**Figure S5)** suggest that the absorber of the selected device is free of secondary phases (neither Se, nor α-$Sb_2O_3$ are detected) and shows good crystal quality with a predominant (002) and (301) texture that implies a preferential [001] orientation (although not uniaxial). Thus, this analysis will focus on the intrinsic properties of the absorber and the interfaces of the device to discriminate among the possible factors limiting its PCE.

**Figure 4** presents the illuminated and dark J-V curves of the selected $Sb_2Se_3$ device. In addition, **Table 2** presents a summary of the most relevant optoelectronic parameters extracted from the J-V analysis as well as from EQE, CV and JV-T measurements. The following information on the figures of merit of the device can be extracted from these data:

- Open circuit voltage: The device presents a $V_{oc}$ of 422 mV. This value is in the range of the best ones reported in the literature (see Table 1). Nevertheless, taking into account that the indirect bandgap of the material is estimated to be 1.26 eV (see Figure 5), a large voltage deficit still exists and should be considered the main limitation of the device (and of $Sb_2Se_3$ devices in general). Such a large $V_{oc}$ deficit can be related either to intrinsic defects, to interface recombination, or to a combination of both.
- Fill Factor: The device exhibits a FF of 61.7 %, which, again, is among the best FF reported in the literature (see Table 1). This is a clear indication of the formation of a good $CdS/Sb_2Se_3$ heterojunction. The low series resistance $R_s$ (2 $\Omega cm^2$), favoured by the [001] preferential orientation of the film (see Figure S5),[18] and the high $R_{sh}$ (1143 $\Omega cm^2$) further support the favourable properties of the heterojunction.
- Short circuit current: In contrast to the $V_{oc}$ and FF, the $J_{sc}$ of this record device (21.9 mA $cm^{-2}$) is low compared to the state of the art of the $Sb_2Se_3$ technology (Table 1). This can be related to the narrow SCR systematically observed in all the samples presented in this work (around 0.212 µm). Furthermore, the low $J_{sc}$ reveals a current leakage problem at the heterojunction that may be pointing towards the degradation of the absorber surface during the deposition of the CdS buffer layer (chemical bath deposition) or even towards an unstable $Sb_2Se_3/CdS$ interface. Figure 4 also shows a clear cross-over between the light and dark J-V curves of the device which is aggravated after first illumination. This can be attributed to the presence of photoactive defects at the $Sb_2Se_3/CdS$ heterojunction interface or within the bulk of the CdS that translate into a high density of acceptor-like traps.[53] These traps can be the

result of partial interface degradation/modification during the CdS or even during the i-ZnO/ITO deposition.

- Regarding other parameters extracted from the dark J-V curve, the reverse saturation current ($J_0$) can be considered relatively high when compared with high PCE chalcogenide devices like CIGS.[54] A high $J_0$ is often related to recombination through interface defects at the p-n junction which supports the idea of $Sb_2Se_3$/CdS interface recombination being one of the main problems of the devices fabricated in this work. On the other hand, the diode quality factor remains below 2 (1.605) which indicates that a single diode model is a reasonably accurate representation of the selected device and that recombination is most probably occurring at the interfaces.
- CV measurements show an apparent carrier concentration of $5.3x10^{16}$ $cm^{-3}$ and a SCR width of 0.212 µm. The carrier concentration is a bit higher than in other works but still compatible with the fabrication of high PCE solar cells.[21,55] On the contrary, the SCR width is narrow, suggesting that either the absorber properties are not optimal, and/or that the SCR width is being influenced by the CdS layer.

Complementary to the previous optoelectronic characterization, external quantum efficiency (EQE), internal quantum efficiency (IQE) and biased IQE measurements were also performed on the record device (**Figure 5a**). The bandgap of the $Sb_2Se_3$ absorber was extracted from the IQE employing the derivative method (**Figure 5b**).[56] A "double feature" is clearly observed which may correspond to the double bandgap (direct and indirect) structure of the material. Values of $E_{g,direct}$ = 1.37 eV and $E_{g,indirect}$ = 1.26 eV were calculated (shown also in Table 2), which are in good agreement with the experimental[24,47,54] and theoretical[57] bandgap values reported in the literature.

On the other hand, the EQE shows a gradual deterioration of charge collection for wavelengths higher than 500 nm. This feature has been previously reported even in high PCE devices.[18] Studying the EQE and IQE curves, it is clear that in the 300-500 nm region the collection losses are mainly

influenced by parasitic absorption on the window/buffer layer and, in the 500-800 nm range to reflections, an increase of the integrated $J_{sc}$ of 2.9 mA $cm^{-2}$ is observed between the IQE and EQE measurements, if we assume a device without reflections the PCE of the device will increase to 6.5%, this could be achieved by the inclusion of an anti-reflective coating. For wavelengths higher than 500 nm (just below the typical bandgap of our CdS),[58] electrical losses become the dominant collection limiting factor as can be deduced from the reverse-biased (-1 V) IQE being considerably higher than the IQE at zero voltage. Considering that under reverse-biased IQE the space charge region (SCR) is being further depleted towards the absorber, the observed difference between the IQE and the reverse-biased IQE points towards an incomplete carrier collection in the 550-1000 nm region. The IQE(-1 V)/IQE(0 V) ratio plot in **Figure 5c** shows a severe deterioration of the collection starting from 600 nm, which indicates that the $Sb_2Se_3$/CdS interface is playing a major role in this issue. This result matches the low SCR width (at 0 V) estimated by CV measurements and could arise from a band mismatch at the p-n interface, non-optimized carrier concentrations and/or high interface recombination at the heterojunction. Similarly, the IQE was also measured under forward bias (+0.4 V, below the flat band voltage which is typically a bit higher than $V_{oc}$) (Figure 5a). The ratio between forward biased and unbiased IQE curves (Figure 5d) shows a relatively constant value, which suggests a good quality absorber. Nevertheless, there is a noticeable reduction for wavelengths below 500 nm that can be associated to recombination at the CdS layer or nearby regions. In particular, for a high photo-generation of charge carriers in the CdS, the higher concentration of holes at the heterojunction can contribute to increasing recombination at the interface. Considering that the absorber exhibits good properties and that the main problems observed in the record sample can be ascribed to the narrow SCR width, these results suggest that the properties of the CdS buffer layer may be significantly affected by the solar cell fabrication process.

**Figure 6a** shows the $V_{oc}$ vs T plot where it can be observed that the linear extrapolation towards 0 K intercepts the y-axis at 0.94 V. This is well below the bandgap of the material determined above from the EQE (1.26 eV) and confirms that the device is bulk and/or interface limited. Thus, further

optimization of the $Sb_2Se_3$/CdS heterojunction is required. **Figure 6b** presents the Urbach energy ($E_U$) of the device (estimated from the IQE as presented in **Equation S1**). The $E_U$ is related to structure/composition/temperature disorder,[59] and manifests itself as tail states or potential fluctuations in the materials.[57] Surprisingly, the $E_U$ found is very low (17.4 meV). This is at the same level or even lower than that of other high PCE chalcogenide materials such as CIGS and CZTSe.[60–62] This indicates that the absorber itself does not present severe disorder problems, and that recombination at the heterojunction arises from a combined effect of the $Sb_2Se_3$ absorber and the CdS buffer.

Therefore, all the previous data suggest that there is a strong modification of the $Sb_2Se_3$/CdS interface during processing, and that this interface is largely limiting the PCE of the devices. Alternative n-type buffer layers have been employed in the literature, although the best reported values are still observed with CdS. This is probably related to the fact that CdS has been extensively researched by the photovoltaic community. As such, we believe that investigating strategies such as barrier layer between CdS and $Sb_2Se_3$ may be a better approach that can help avoiding interface instability in $Sb_2Se_3$/CdS and lead to further development of this technology.

## 3. Conclusion

This work proves the feasibility of synthesizing photovoltaic quality $Sb_2Se_3$ layers using a sequential process based on reactive annealing under Se atmosphere of elemental Sb layers deposited by thermal evaporation. This technique has been demonstrated to be well suited for an accurate control of the 3[Sb]/2[Se] ratio in the Se-rich part of the phase diagram by varying the annealing temperature and the relevance of this parameter in the device optoelectronic performance. In this work has been presented a deep study on the effects of selenium content in the performance of Se-rich $Sb_2Se_3$/CdS planar heterojunction solar cells and an in deep characterization of the best performing device obtained to shed light of their main limiting factors. Medium and high Se-excess have been found to increase the shunt resistance of the devices although the highest contents have been observed to affect

the $Sb_2Se_3$ heterojunction. However, through a compositional tuning (3[Sb]/2[Se] = 0.88), a champion solar cell device with PCE = 5.7 %, FF = 61.7 %, $V_{oc}$ = 422 mV and $J_{sc}$ = 21.9 mA $cm^{-2}$ has been obtained that could potentially be increased to 6.5% using an anti-reflecting in the structure. Finally, further JV-T and QE measurements in our record devices suggests that the main limiting factor of this technology is the heterojunction.

## 4. Experimental Section

*Device Preparation:* 10 x 10 $cm^2$ soda-lime glass (SLG) substrates were cleaned with soap and then submitted to a 3-step ultrasonic bath cleaning in acetone, isopropanol, deionized water (18.2 MΩ), for a duration of 10 min each, and dried with argon. The clean glasses were then coated with a Molybdenum tri-layer structure (around 800 nm full thickness), using a DC-magnetron sputtering machine (Alliance Concept AC450). The Mo tri-layer is composed by a first named MoA layer (500 nm) deposited at higher power (4.2 W $cm^{-2}$) and low pressure ($1.3 \cdot 10^{-3}$ mbar), a second named MoB layer (250 nm), resistant to selenization, deposited at lower power (2.8 W $cm^{-2}$) and higher pressure ($5.0 \cdot 10^{-3}$ mbar), and finally a third MoA layer (50 nm) used for sacrificial purposes with the same characteristics as the first one, the total sheet resistance of the tri-layer being ~0.3 Ω $sq^{-1}$.[51] A thin Sb metallic layer was then deposited by thermal evaporation (Oerlikon Univex 250) from elemental powder (Alfa Aesar, 99.5%) using a tungsten boat (10 rpm, rate of 0.6 Å $s^{-1}$, power ~57.4 W, base pressure ~$10^{-5}$ mbar). The thickness of the Sb layers was determined by X-ray fluorescence spectroscopy (XRF) (Fisherscope XDV) being 250 ± 10 nm, which was previously calibrated with several samples of known thicknesses. The samples were then cut in pieces of 1.25 x 2.5 $cm^2$ and were annealed in a 3-zone tubular furnace using a graphite box (26.5 $cm^3$ volume) containing 25 mg of selenium powder (Alfa Aesar Puratronic®, 99.9995%), the tube was filled with argon to provide an inert atmosphere and to control the system pressure. Several thermal processes were performed at different temperatures, times and pressures as described throughout the main text. In all the cases, the

heating ramp was 20 ºC $min^{-1}$ and the cooling down to room temperature was allowed to occur naturally (around 1 hour).

The heterojunction was then completed with an n-type CdS buffer layer (50 nm) deposited by chemical bath deposition, being the Cd source $Cd(NO_3)_2$, with conditions [Cd $(NO_3)_2$] = 0.12 M, [Thiourea] 0.3 M, pH= 9.5, T= 80 °C.[58] The front transparent conductive window layer formed by i-ZnO (50 nm) and $In_2O_3$:$SnO_2$ (90/10 wt. %) (150 nm) layers were deposited by DC-pulsed magnetron sputtering (Alliance Concept CT100) at 200 ºC. Individual solar cells (3x3 $mm^2$) were then insulated using a manual mechanical scriber (Micro Diamond MR200 OEG) with a scribed line width of 20 µm.

*Film and Device Characterization:* The composition of the absorber layers was determined with an XRF equipment (Fischerscope XVD) calibrated by inductively coupled plasma (ICP), the measurements were carried out in a 4 × 4 points grid covering the full area of the individual 3x3 mm cells using a 50 kV accelerating voltage, a Ni10 filter to reduce background signal, and an integration time per measuring point of 45 s. Scanning electron microscopy (SEM) micrographs were acquired in cross-section configuration (by mechanical cleavage of the full samples) using a Zeiss Series Auriga field emission equipment, an acceleration voltage of 5 kV and working distances ranging between 3 to 5 depending on the sample. Raman scattering measurements were performed using a Raman probe developed at IREC coupled with optical fiber to an FHR640 Horiba Jobin Yvon spectrometer and in back scattering configuration using 633 nm excitation wavelength with the laser spot focused onto the surface. The measurements were performed using a laser power density below 10 $W/cm^2$ and using a macro-spot with a diameter of around 50 µm. X-ray diffraction (XRD) patterns were obtained using a Bruker D8 Advance equipment in Bragg Brentano configuration from 10º to 90º degrees with a step size of 0.02º and using a one-dimensional detector, for the Rietveld analysis of the best device results were obtained with a PANalytical X'Pert PRO MPD Bragg-Brentano powder diffractometer equipped with a Cu tube operating at 45 kV and 40 mA, a Ge (111) Johansson type primary focalizing monochromator and a silicon strip 1D X'Celerator detector. High resolution,

high statistics, full angular range Cu Kα1 θ/2θ scans are obtained: 2θ/θ scans from 4 to 145°. Current density-voltage (J-V) measurements were performed on complete devices using a Sun 3000 AAA solar simulator from Abet Technology (uniform illumination area of 15 x 15 $cm^2$) calibrated with a Si reference solar cell under AM1.5 illumination. Quantum efficiency (QE) measurements were carried out with a Bentham PVE300 spectral response system in the 300-1600 nm range calibrated with Si and Ge reference photodiodes.

Capacitance-voltage (CV) measurements were performed with a Keysight E4990A impedance analyser and a homemade faraday cage 4-probe setup. Samples were kept in dark conditions during the measurement. The measurements were performed in a voltage range between [-1, +0.3] V. Selected frequency for data analysis was chosen to be 10 KHz. The equivalent circuit model employed is composed of a series resistance, a parallel resistance and a capacitor. Dielectric constant was fixed to 19 based on bibliography ellipsometry measurements, although the reported values assume a very complex dielectric constant and thus the values for carrier concentration will be referred as apparent.[19,50]

Current density-voltage-temperature (JV-T) analysis was performed by introducing the sample into a cryostat (Cold-Head model RDK-101D Sumitamo Heavy Industries Ltd.) cooled by a Helium closed cycle compressor (Zephyr HC-4A from Sumitamo cryogenics). Samples were illuminated with a solar simulator (Oriel LCS AM1.5 model 94011A). Samples were attached with silver paste to the cold finger and a temperature sensor was placed aside on top of a 3 mm soda lime glass piece to mimic the conditions of the film. Electrical contacts were performed on a 4-probe configuration, two of them connected to the indium-covered Mo back contact and the other two to the front ITO contact by applying silver paste. The range of temperatures probed was from 300-145 K (until $V_{oc}$ saturation). Pressure was controlled by a turbo-molecular pump (Varian Mini-TASK AG81) with base vacuum of ~$10^{-6}$ mbar.

**Supporting Information**

Supporting Information is available from the Wiley Online Library or from the author.

**Acknowledgements**

This project has received funding from the European Union's Horizon 2020 research and innovation programme under the Marie Skłodowska-Curie grant agreement No 712949 (TECNIOspring PLUS) and the Government of Catalonia's Agency for Business Competitiveness (ACCIÓ). This research has also been supported by the H2020 Programme under the project INFINITE-CELL (grant no. H2020-MSCA-RISE-2017-777968), by the DURACIS project from the SOLARERANET International program (subproject ref. PCIN-2017-041 funded by Spanish MINECO), by the Spanish Ministry of Science, Innovation and Universities under the WINCOST (grant no. ENE2016-80788-C5-1-R), and by the European Regional Development Funds (ERDF, FEDER Programa Competitivitat

Received: ((will be filled in by the editorial staff))
Revised: ((will be filled in by the editorial staff))
Published online: ((will be filled in by the editorial staff))

**References**

[1] M. A. Green, Y. Hishikawa, E. D. Dunlop, D. H. Levi, J. Hohl-Ebinger, M. Yoshita, A. W. Y. Ho-Baillie, *Prog. Photovoltaics Res. Appl.* **2019**, 27, 3.

[2] V. Bermudez, A. Perez-Rodriguez, *Nat. Energy* **2018**, 3, 466.

[3] A. Zuser, H. Rechberger, *Resour. Conserv. Recycl.* **2011**, 56, 56.

[4] V. Fthenakis, *Renew. Sustain. Energy Rev.* **2009**, 13, 2746.

[5] D.-H. Son, S.-H. Kim, S.-Y. Kim, Y.-I. Kim, J.-H. Sim, S.-N. Park, D.-H. Jeon, D.-K. Hwang, S.-J. Sung, J.-K. Kang, K.-J. Yang, D.-H. Kim, *J. Mater. Chem. A.* 7 (**2019**) 25279–25289.

[6] Lydia H. Wong, A. Zakutayev, J. D. Major, X. Hao, A. Walsh, T. K. Todorov, E. Saucedo, *J. Phys. Energy* **2019**, DOI 10.1088/2515-7655/ab2338.

[7] B. Krishnan, S. Shaji, R. Ernesto Ornelas, *J. Mater. Sci. Mater. Electron.* **2015**, 26, 4770.

[8] A. Kanai, K. Toyonaga, K. Chino, H. Katagiri, H. Araki, *Jpn. J. Appl. Phys.* **2015**, 54, 08KC06.

[9] A. Zakutayev, *Curr. Opin. Green Sustain. Chem.* **2017**, 4, 8.

[10] F. Oliva, L. Arqués, L. Acebo, M. Guc, Y. Sánchez, X. Alcobé, A. Pérez-Rodríguez, E. Saucedo, V. Izquierdo-Roca, *J. Mater. Chem. A* **2017**, 5, 23863.

[11] D. J. Xue, B. Yang, Z. K. Yuan, G. Wang, X. Liu, Y. Zhou, L. Hu, D. Pan, S. Chen, J. Tang, *Adv. Energy Mater.* **2015**, 5, 1.

*[12]* P. Sinsermsuksakul, L. Sun, S. W. Lee, H. H. Park, S. B. Kim, C. Yang, R. G. Gordon, *Adv. Energy Mater.* **2014**, 4, 1400496.

[13] D. Lee, J. Y. Cho, H. S. Yun, D. K. Lee, T. Kim, K. Bang, Y. S. Lee, H. Y. Kim, J. Heo, *J. Mater. Chem. A* **2019**, 7, 7186.

*[14]* D. J. Xue, S. C. Liu, C. M. Dai, S. Chen, C. He, L. Zhao, J. S. Hu, L. J. Wan, *J. Am. Chem. Soc.* **2017**, 139, 958.

[15] H. Lei, J. Chen, Z. Tan, G. Fang, *Sol. RRL* **2019**, 1900026, 1900026.

[16] T. K. Todorov, S. Singh, D. M. Bishop, O. Gunawan, Y. S. Lee, T. S. Gershon, K. W. Brew, P. D. Antunez, R. Haight, *Nat. Commun.* **2017**, 8, DOI 10.1038/s41467-017-00582-9.

[17] I. Hadar, T. Bin Song, W. Ke, M. G. Kanatzidis, *Adv. Energy Mater*. **2019**, 9, 1.

[18] Z. Li, X. Liang, G. Li, H. Liu, H. Zhang, J. Guo, J. Chen, K. Shen, X. San, W. Yu, R. E. I. Schropp, Y. Mai, *Nat. Commun*. **2019**, 10, 125.

[19] C. Chen, D. C. Bobela, Y. Yang, S. Lu, K. Zeng, C. Ge, B. Yang, L. Gao, Y. Zhao, M. C. Beard, J. Tang, *Front. Optoelectron*. **2017**, 10, 18.

[20] Y. Zhou, L. Wang, S. Chen, S. Qin, X. Liu, J. Chen, D. J. Xue, M. Luo, Y. Cao, Y. Cheng, E. H. Sargent, J. Tang, *Nat. Photonics* **2015**, 9, 409.

[21] Z. Li, X. Chen, H. Zhu, J. Chen, Y. Guo, C. Zhang, W. Zhang, X. Niu, Y. Mai, *Sol. Energy Mater. Sol. Cells* **2017**, 161, 190.

[22] R. Kondrotas, J. Zhang, C. Wang, J. Tang, *Sol. Energy Mater. Sol. Cells* **2019**, 199, 16.

[23] F. Oliva, S. Kretzschmar, D. Colombara, S. Tombolato, C. M. C. M. Ruiz, A. Redinger, E. Saucedo, C. Broussillou, T. G. T. G. de Monsabert, T. Unold, P. J. P. J. Dale, V. Izquierdo-Roca, A. Pérez-Rodríguez, *Sol. Energy Mater. Sol. Cells* **2016**, 158, 168.

*[24]* M. Dimitrievska, A. Fairbrother, E. Saucedo, A. Pérez-Rodríguez, V. Izquierdo-Roca, *Sol. Energy Mater. Sol. Cells* **2016**, 149, 304.

[25] X. Liu, J. Chen, M. Luo, M. Leng, Z. Xia, Y. Zhou, S. Qin, D. J. Xue, L. Lv, H. Huang, D. Niu, J. Tang, *ACS Appl. Mater. Interfaces* **2014**, 6, 10687.

[26] X. Liu, X. Xiao, Y. Yang, D. J. Xue, D. B. Li, C. Chen, S. Lu, L. Gao, Y. He, M. C. Beard, G. Wang, S. Chen, J. Tang, *Prog. Photovoltaics Res. Appl.* **2017**, 25, 861.

[27] G. Li, Z. Li, X. Liang, C. Guo, K. Shen, Y. Mai, *ACS Appl. Mater. Interfaces* **2019**, 11, 828.

[28] Y. Z. and J. T. Xinsheng Liu, Chao Chen, Liang Wang, Jie Zhong, Miao Luo, Jie Chen, Ding-Jiang Xue, Dengbing Li, *Prog. Photovoltaics* **2015**, 23, 1828.

[29] X. Wen, Y. He, C. Chen, X. Liu, L. wang, B. Yang, M. Leng, H. Song, K. Zeng, D. Li, K. Li, L. Gao, J. Tang, *Sol. Energy Mater. Sol. Cells* **2017**, 172, 74.

*[30]* K. Li, R. Kondrotas, C. Chen, S. Lu, X. Wen, D. Li, J. Luo, Y. Zhao, J. Tang, *Sol. Energy* **2018**, 167, 10.

[31] X. Hu, J. Tao, S. Chen, J. Xue, G. Weng, Kaijiang, Z. Hu, J. Jiang, S. Chen, Z. Zhu, J. Chu, *Sol. Energy Mater. Sol. Cells* **2018**, 187, 170.

*[32]* X. Hu, J. Tao, G. Weng, J. Jiang, S. Chen, Z. Zhu, J. Chu, *Sol. Energy Mater. Sol. Cells* **2018**, 186, 324.

[33] K. Shen, C. Ou, T. Huang, H. Zhu, J. Li, Z. Li, Y. Mai, *Sol. Energy Mater. Sol. Cells* **2018**, 186, 58.

[34] L. J. Phillips, C. N. Savory, O. S. Hutter, P. J. Yates, H. Shiel, S. Mariotti, L. Bowen, M. Birkett, K. Durose, D. O. Scanlon, J. D. Major, *IEEE J. Photovoltaics* **2019**, 9, 544.

[35] J. Zhang, R. Kondrotas, S. Lu, C. Wang, C. Chen, *J. Tang, Sol. Energy* **2019**, 182, 96.

[36] M. Leng, M. Luo, C. Chen, S. Qin, J. Chen, J. Zhong, J. Tang, *Appl. Phys. Lett.* **2014**, 105, DOI 10.1063/1.4894170.

*[37]* C. Chen, K. Li, S. Chen, L. Wang, S. Lu, Y. Liu, D. Li, H. Song, J. Tang, *ACS Energy Lett.* **2018**, 3, 2335.

[38] H. Guo, Z. Chen, X. Wang, Q. Cang, X. Jia, C. Ma, N. Yuan, J. Ding, *Sol. RRL* **2019**, 3, 1970033.

[39] Z. Li, H. Zhu, Y. Guo, X. Niu, X. Chen, C. Zhang, W. Zhang, X. Liang, D. Zhou, J. Chen, Y. Mai, *Appl. Phys. Express* **2016**, 9, DOI 10.7567/APEX.9.052302.

[40] C. Yuan, L. Zhang, W. Liu, C. Zhu, *Sol. Energy* **2016**, 137, 256.

[41] X. Wen, C. Chen, S. Lu, K. Li, R. Kondrotas, Y. Zhao, W. Chen, L. Gao, C. Wang, J. Zhang, G. Niu, J. Tang, *Nat. Commun*. **2018**, 9, 2179.

[42] C. Chen, Y. Zhao, S. Lu, K. Li, Y. Li, B. Yang, W. Chen, L. Wang, D. Li, H. Deng, F. Yi, J. Tang, *Adv. Energy Mater*. **2017**, 7, 1.

[43] D. B. Li, X. Yin, C. R. Grice, L. Guan, Z. Song, C. Wang, C. Chen, K. Li, A. J. Cimaroli, R. A. Awni, D. Zhao, H. Song, W. Tang, Y. Yan, J. Tang, *Nano Energy* **2018**, 49, 346.

[44] C. Chen, L. Wang, L. Gao, D. Nam, D. Li, K. Li, Y. Zhao, C. Ge, H. Cheong, H. Liu, H. Song, J. Tang, *ACS Energy Lett.* **2017**, 2, 2125.

[45] L. Wang, D. B. Li, K. Li, C. Chen, H. X. Deng, L. Gao, Y. Zhao, F. Jiang, L. Li, F. Huang, Y. He, H. Song, G. Niu, J. Tang, *Nat. Energy* **2017**, 2, 1.

[46] C. Yuan, X. Jin, G. Jiang, W. Liu, C. Zhu, *J. Mater. Sci. Mater. Electron.* **2016**, 27, 8906.

[47] P. Vidal-Fuentes, M. Guc, X. Alcobe, T. Jawhari, M. Placidi, A. Pérez-Rodríguez, E. Saucedo, V.I. Roca, *2D Mater*. 6 (**2019**) 045054. doi:10.1088/2053-1583/ab4029.

[48] M. Huang, P. Xu, D. Han, J. Tang, S. Chen, *ACS Appl. Mater. Interfaces* **2019**, 11, 15564.

[49] T. Cebriano, B. Méndez, J. Piqueras, *Mater. Chem. Phys.* **2012**, 135, 1096.

[50] C. Chen, W. Li, Y. Zhou, C. Chen, M. Luo, X. Liu, K. Zeng, B. Yang, C. Zhang, J. Han, J. Tang, *Appl. Phys. Lett.* 107 (**2015**) 043905. doi:10.1063/1.4927741.

[51] S. Lopez-Marino, M. Espíndola-Rodríguez, Y. Sánchez, X. Alcobé, F. Oliva, H. Xie, M. Neuschitzer, S. Giraldo, M. Placidi, R. Caballero, V. Izquierdo-Roca, A. Pérez-Rodríguez, E. Saucedo, **Nano Energy 2016**, 26, 708.

[52] M. Neuschitzer, J. Marquez, S. Giraldo, M. Dimitrievska, M. Placidi, I. Forbes, V. Izquierdo-Roca, A. Pérez-Rodriguez, E. Saucedo, *J. Phys. Chem. C* **2016**, 120, 9661.

[53] M. Neuschitzer, Y. Sanchez, S. Lopez-Marino, H. Xie, A. Fairbrother, M. Placidi, S. Haass, V. Izquierdo-Roca, A. Perez-Rodriguez, E. Saucedo, *Prog. Photovoltaics Res. Appl.* **2015**, 23, 1660.

[54] S. R. Kodigala, in *Thin Film. Nanostructures*, **2010**, pp. 505–679.

[55] M. Luo, M. Leng, X. Liu, J. Chen, C. Chen, S. Qin, *J. Tang, Appl. Phys. Lett.* **2014**, 104, DOI 10.1063/1.4874878.

[56] R. Carron, C. Andres, E. Avancini, T. Feurer, S. Nishiwaki, S. Pisoni, F. Fu, M. Lingg, Y. E. Romanyuk, S. Buecheler, A. N. Tiwari, *Thin Solid Films* **2019**, 669, 482.

[57] R. Vadapoo, S. Krishnan, H. Yilmaz, C. Marin, *Phys. Status Solidi Basic Res.* **2011**, 248, 700.

[58] M. Neuschitzer, Y. Sanchez, S. Lõpez-Marino, H. Xie, A. Fairbrother, M. Placidi, S. Haass, V. Izquierdo-Roca, A. Perez-Rodriguez, E. Saucedo, *Prog. Photovoltaics Res. Appl.* **2015**, 23, 1660.

[59] I. Studenyak, M. Kranj, M. Kurik, *Int. J. Opt. Appl.* **2014**, 4, 76.

[60] J. P. Teixeira, P. M. P. Salomé, B. Alves, M. Edoff, J. P. Leitão, *Phys. Rev. Appl.* **2019**, 11, 054013.

[61] M. Neuschitzer, M. Espindola-Rodriguez, M. Guc, J. Marquez, S. Giraldo, I. Forbes, A. Perez-Rodriguez, E. Saucedo, *J. Mater. Chem. A* **2018**, 6, 11759.

[62] S. Lopez-Marino, Y. Sánchez, M. Placidi, A. Fairbrother, M. Espindola-Rodríguez, X. Fontané, V. Izquierdo-Roca, J. Lopez-García, L. Calvo-Barrio, A. Pérez-Rodríguez, E. Saucedo, *Chem. - A Eur. J.* **2013**, 19, 14814.

[63] S. Lopez-Marino, M. Espíndola-Rodríguez, Y. Sánchez, X. Alcobé, F. Oliva, H. Xie, M. Neuschitzer, S. Giraldo, M. Placidi, R. Caballero, V. Izquierdo-Roca, A. Pérez-Rodríguez, E. Saucedo, **Nano Energy 2016**, 26, 708.

[64] C. Chen, W. Li, Y. Zhou, C. Chen, M. Luo, X. Liu, K. Zeng, B. Yang, C. Zhang, J. Han, J. Tang, *Appl. Phys. Lett.* 107 (**2015**) 043905. doi:10.1063/1.4927741.

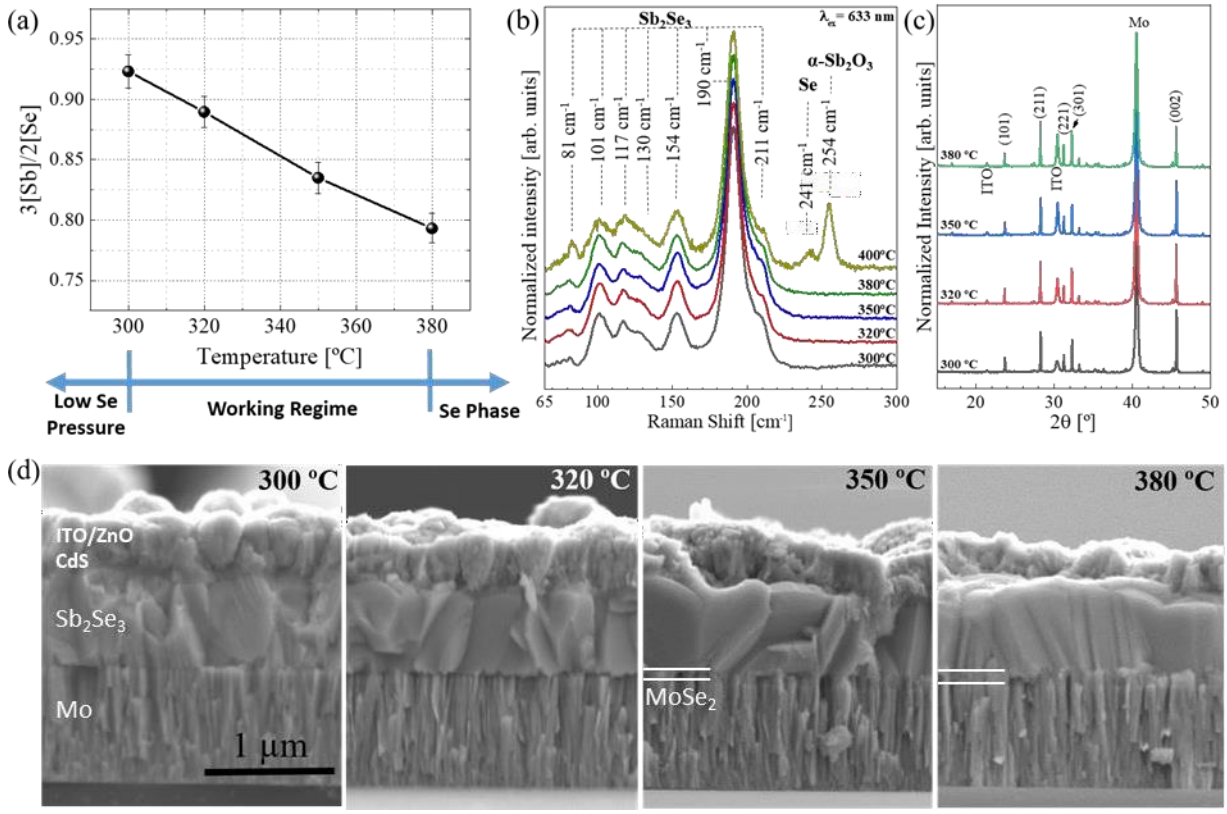


**Figure 1.** Effect of synthesis temperature on $Sb_2Se_3$ absorber layers: (a) Compositional ratio 3[Sb]/2[Se] obtained at different temperatures showing an optimal range (working regime) comprised between 300-380 ºC. (b) Raman spectra ($\lambda_{ex}$ = 633 nm) showing the presence of Se and α-$Sb_2O_3$ for the absorber processed at 400 ºC. (c) XRD diffractograms with preferential orientation around [001] for all the temperatures. (d) Cross-section SEM images of the samples processed at different temperatures.

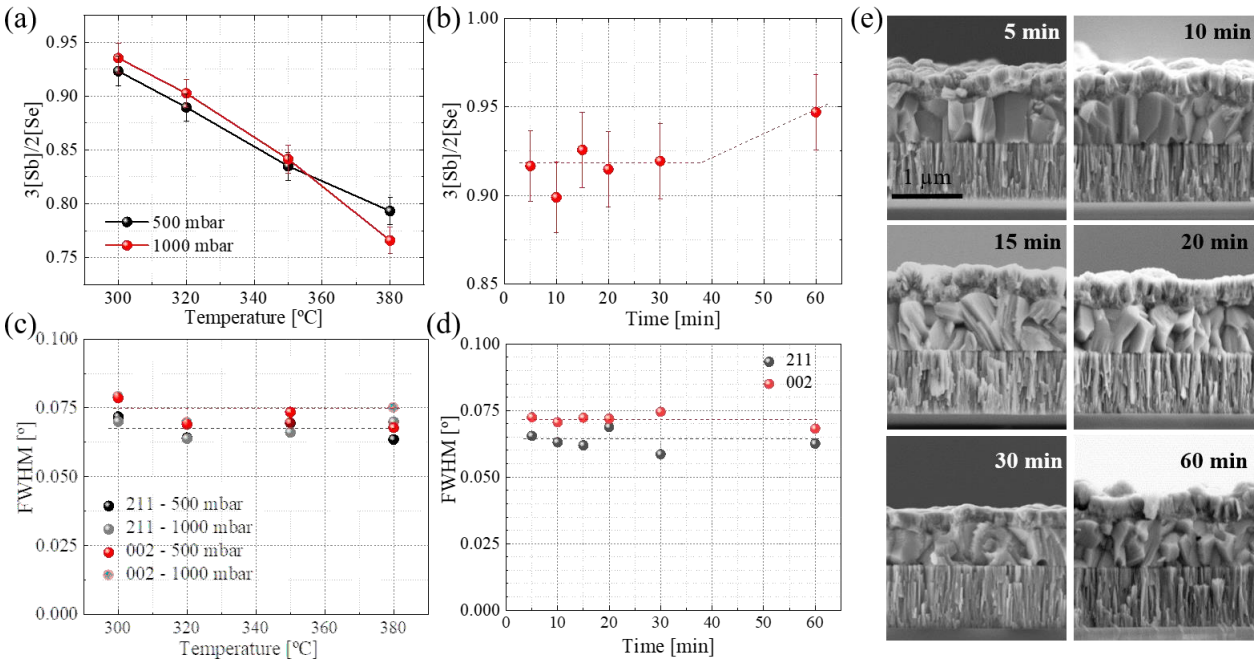


**Figure 2.** Effect of the pressure and time for the synthesis of the $Sb_2Se_3$ absorber layers: (a) and (b) Composition ratios dependence with pressure and time. (c) and (d) FWHM dependence with pressure and time of the 002 and 211 reflections. (e) Cross-section SEM images of the samples for different processing times.

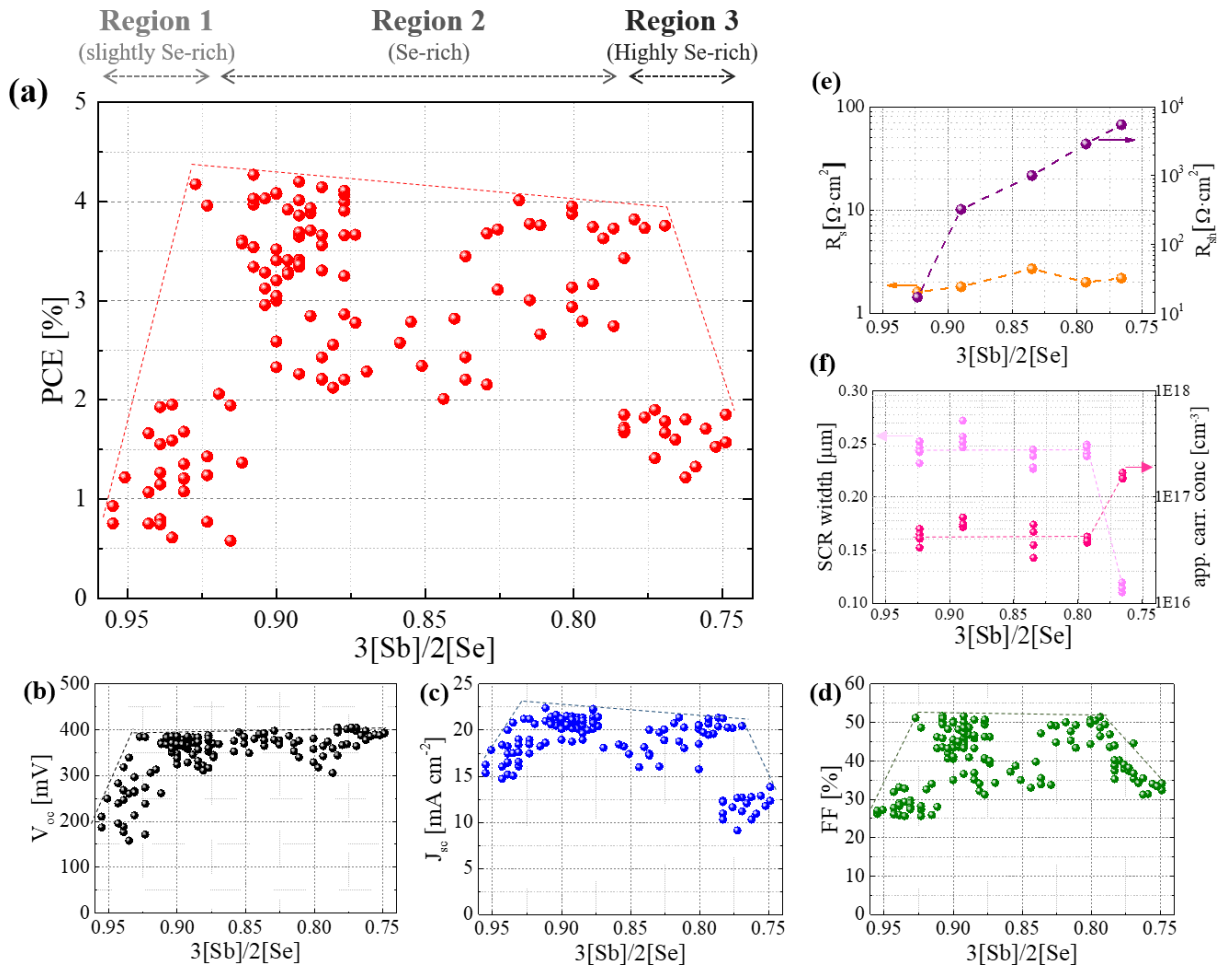


**Figure 3.** Effect of the composition on the device performance of $Sb_2Se_3$/CdS planar heterojunction solar cells: (a) power conversion efficiency; (b) open circuit voltage; (c) short circuit current; (d) fill factor; (e) series and shunt resistances; and (f) apparent carrier concentration and space charge region width, as a function of the 3[Sb]/2[Se] composition ratio.

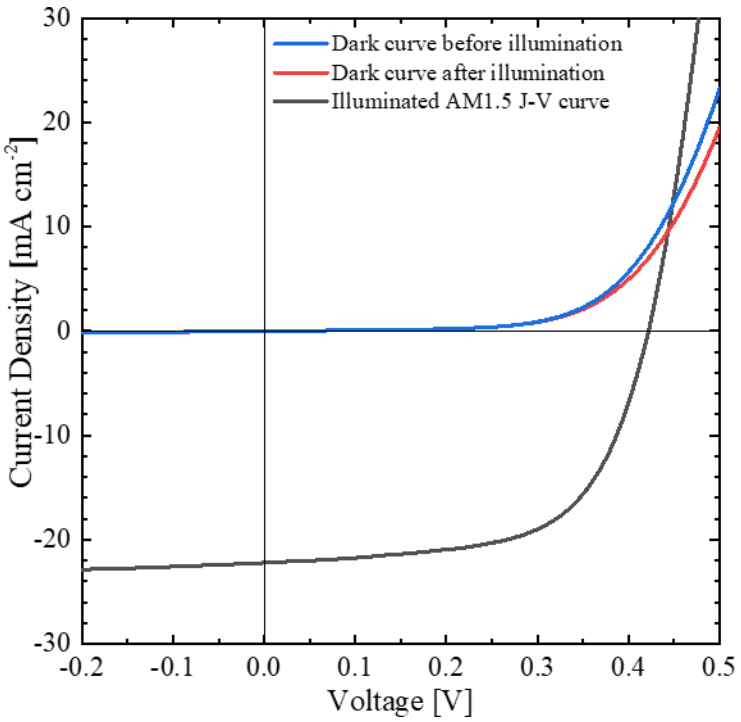


**Figure 4.** Dark and illuminated J-V characteristics of the best solar cell obtained in this study.

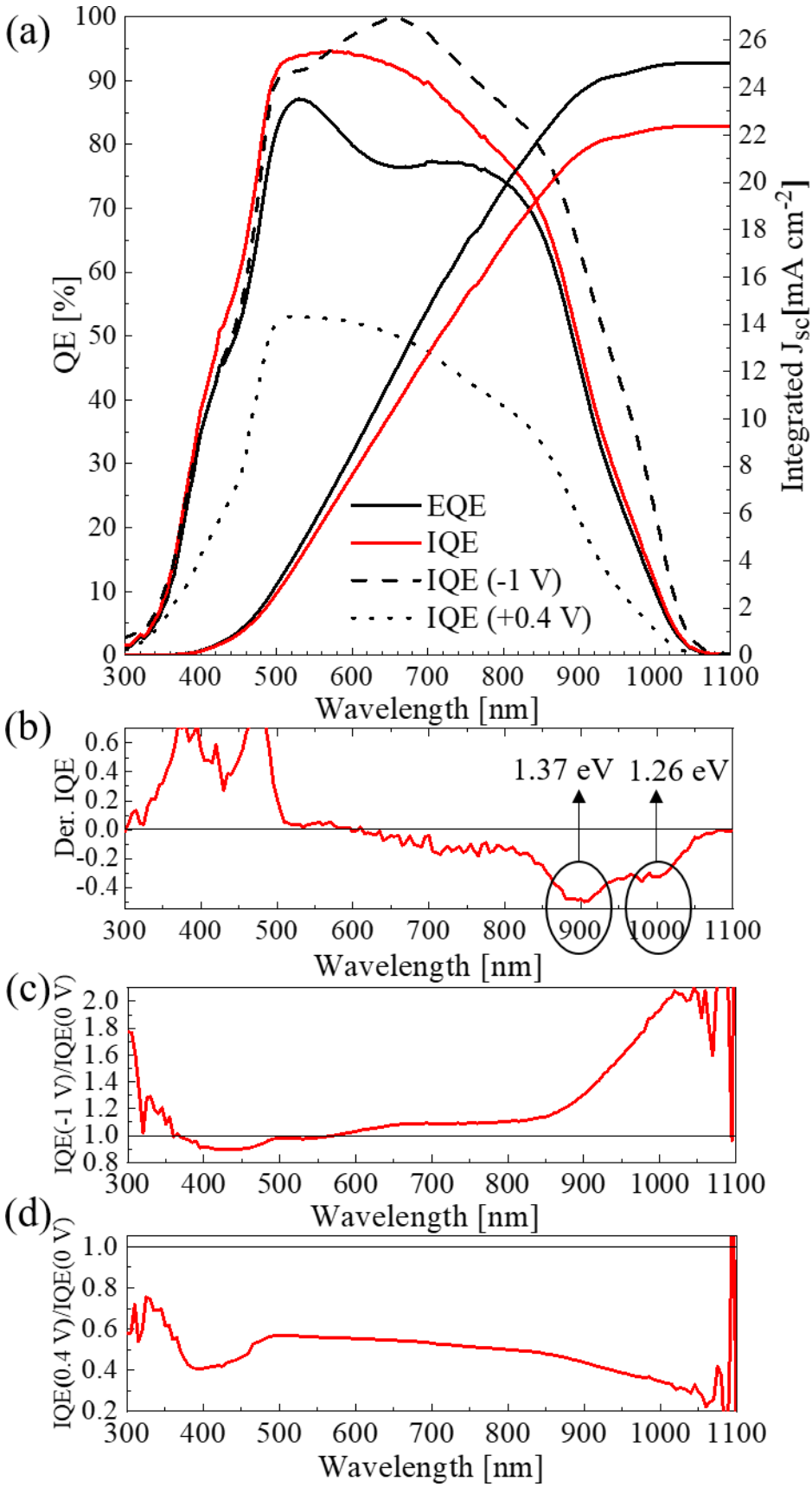


**Figure 5.** Spectral response characterization of the best device: (a) External, Internal and biased Internal (reverse at -1 V and forward at +0.4 V) quantum efficiency, along with the integrated $J_{sc}$ for EQE and IQE. (b) Bandgap calculation from the derivative method. (c) Ratio between IQE(-1 V)/IQE(0 V). (d) Ratio between IQE(+0.4 V)/IQE(0 V).

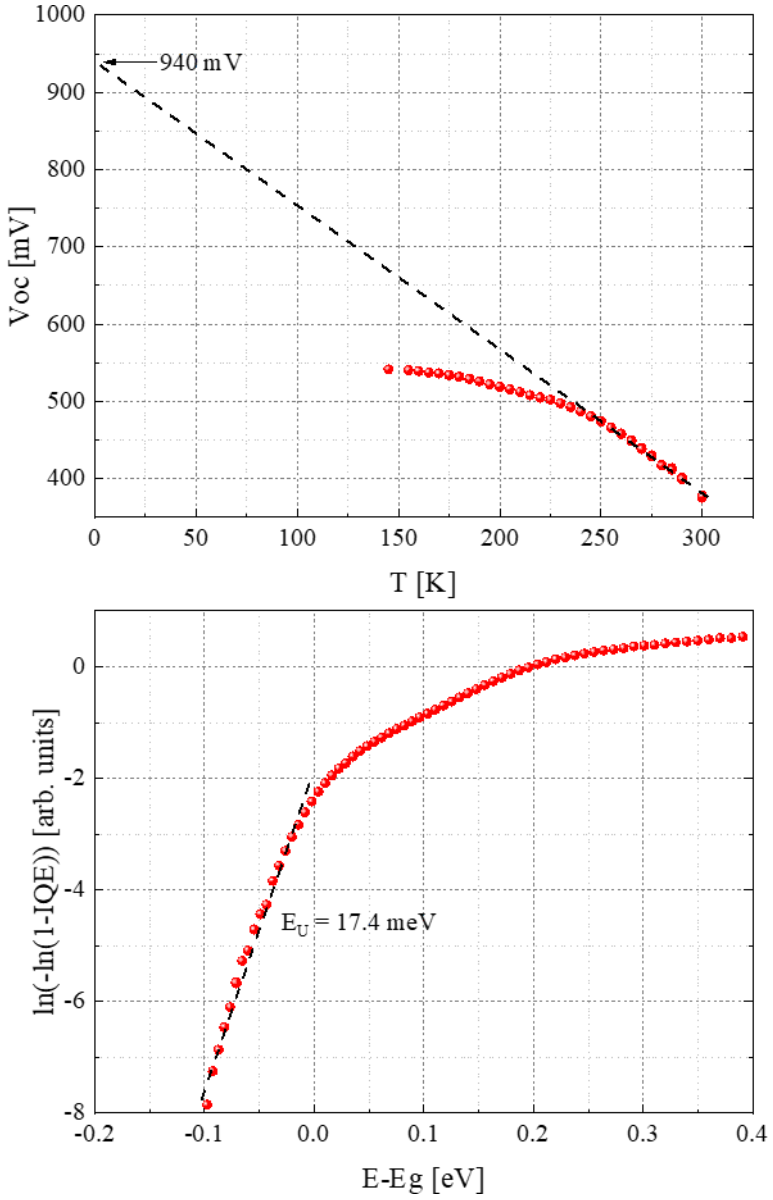


**Figure 6.** (a) $V_{oc}$ vs T plot. (b) Urbach plot for the determination of $E_U$ from the IQE.

**Table 1.** Summary of the best planar $Sb_2Se_3$ solar cells (Works using organic layers as HTL have not been reported in the table).

| Ref. | Technique | Configuration | Device structure | Eff. (%) | FF (%) | $J_{sc}$ (mA/cm²) | $V_{oc}$ (mV) | Comments |
|---|---|---|---|---|---|---|---|---|
| 37 | RTE[a)] | SS[g)] | Glass/ITO/CdS/$Sb_2Se_3$/Au | 7.04 | 59.3 | - | - | $CuCl_2$ treatment+ $(NH_4)_2S$ etching |
| 21 | TE[b)] | S[h)] | SLG/Mo/$MoSe_2$/$Sb_2Se_3$/CdS/ZnO/ITO/Au | 4.25 | 58.1 | 17.1 | 427 | Mo selenization |
| 39 | CE[c)] | SS | SLG/FTO/CdS//$Sb_2Se_3$/Au | 3.47 | 41.3 | 23.1 | 364 | |
| 40 | RTP[d)] | S | SLG/Mo/$Sb_2Se_3$/CdS/Al/ZnO:Al | 3.47 | 52 | 16.0 | 414 | |
| 41 | VTD[e)] | SS | Glass/ITO/CdS/$Sb_2Se_3$/Au | 7.6 | 60.4 | 29.9 | 420 | |
| 42 | RTE | SS | Glass/FTO/$TiO_2$/$Sb_2Se_3$/Au | 5.6 | 55.1 | 28.3 | 358 | $(NH_4)_2S$ etching |
| 43 | CSS[f)] | SS | Glass/FTO/CdS/Glass $Sb_2Se_3$/CZ-TA/Au | 6.84 | 57.1 | 28.4 | 421 | n-i-p structure |
| 44 | RTE | SS | Glass/ITO/CdS/$Sb_2Se_3$/PbS(CQD)/Au | 6.5 | 59.3 | 25.5 | 427 | n-i-p structure |
| 45 | RTE | SS | Glass/FTO/ZnO/$Sb_2Se_3$/Au | 5.93 | 57.8 | 26.2 | 391 | ZnO orientation control |
| 27 | CSS | S | SLG/Mo/$Sb_2Se_3$/$Cd_xZn_{1-x}S$/ZnO/ZnO:Al | 6.71 | 64.8 | 25.7 | 403 | |
| 28 | TE | SS | Glass/ITO/CdS/$Sb_2Se_3$/Au | 4.8 | 52.5 | 25.3 | 353 | $O_2$ addition |
| 29 | RTE | SS | Glass/FTO/ZnO/$Sb_2Se_3$/Au | 4.08 | 44.5 | 28.0 | 328 | Air annealed |
| 30 | RTE | SS | Glass/FTO/ZnO/$Zn_{1-x}Mg_xO$/$Sb_2Se_3$/Au | 4.45 | 48.0 | 26.2 | 360 | $Zn_{0.9}Mg_{0,1}O$ |
| 31 | VTD | SS | Glass/ITO/CdS/$Sb_2Se_3$/Au | 5.72 | 55.7 | 26.0 | 371 | Post annealing in vacuum 200ºC |
| 32 | VTD | SS | Glass/ITO/$SnO_2$/CdS/ $Sb_2Se_3$/Au | 5.91 | 58.4 | 27.3 | 355 | |
| 33 | CSS | SS | Glass/FTO/$SnO_2$/CdS/ $Sb_2Se_3$/Au | 5.18 | 55.0 | 24.5 | 385 | |
| 34 | CSS | SS | Glass/FTO/$TiO_2$/ $Sb_2Se_3$/Au | 5.5 | 49.0 | 25.4 | 450 | $TiO_2$ buffer |
| 35 | VTD | SS | Glass/ITO/CdS/ $Sb_2Se_3$/Au | 7.0 | 57 | 29.4 | 417 | $NiO_x$ back contact proof of concept |
| 36 | TE | SS | Glass/FTO/CdS/ $Sb_2Se_3$/Au | 3.7 | 46.8 | 24.4 | 335 | Post selenization |
| 38 | RTE | SS | Glass/FTO/CdS/p- $Sb_2Se_3$/p+ $Sb_2Se_3$/$Al_2O_3$/Au | 6.7 | 57.8 | 28.6 | 406 | Oxygen plasma + $A_{l2}O_3$ |
| 18 | CSS | S | Glass/Mo/$MoSe_2$/ $Sb_2Se_3$-nanorods/$TiO_2$/CdS/ZnO/AZO | 9.2 | 70.3 | 32.6 | 400 | Nanorod $Sb_2Se_3$ + ALD $TiO_2$ |

a) Rapid thermal evaporation; b) Thermal evaporation; c) Co-evaporation; d) Rapid thermal process; e) Vapor transport deposition; f) Close space sublimation; g) superstrate; h) substrate.

**Table 2.** Summary of the optoelectronic parameters obtained for the champion solar cell obtained in this study. The parameters are extracted from Figure 4, 5 and 6

| **Parameter** | **Value** | **[units]** |
|---|---|---|
| 3[Sb]/2[Se] | 0.88 | - |
| PCE | 5.7 | % |
| $V_{oc}$ | 422 | mV |
| $J_{sc}$ | 21.9 | mA $cm^{-2}$ |
| F.F. | 61.7 | % |
| $R_s$ | 2 | $\Omega cm^2$ |
| $R_{sh}$ | 1143 | $\Omega cm^2$ |
| $J_0$ | 0.001 | mA $cm^{-2}$ |
| A | 1.605 | - |
| App. carr. conc. | $5.3x10^{16}$ | $cm^{-3}$ |
| SCR | 212 | nm |
| $E_{g,ind}$ | 1.26 | eV |
| $E_{g,dir}$ | 1.37 | eV |
| $E_U$ | 17.4 | meV |
| Ext. $V_{oc}$ (0 K) | 0.94 | eV |

A sequential process for the synthesis of Q-1D $Sb_2Se_3$ solar cell absorbers is presented, and the annealing temperature is found as the main parameter controlling the composition of the Se-rich layers. A systematic study of the evolution of the optolectronic parameters of the solar cells as a function of the Se excess is presented identifying the main efficiency limiting factors.

**Keyword: Q1-D $Sb_2Se_3$ solar cells**

**P. Vidal-Fuentes, M. Placidi, Y. Sánchez, I. Becerril-Romero, J. Andrade-Arvizu, Z. Jehl, A. Pérez-Rodríguez, V. Izquierdo-Roca, E. Saucedo***

**Efficient Se-rich $Sb_2Se_3$/CdS planar-heterojunction solar cells by sequential processing: control and influence of Se content**

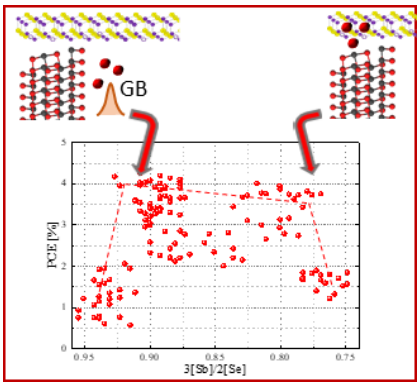


Copyright WILEY-VCH Verlag GmbH & Co. KGaA, 69469 Weinheim, Germany, 2018.

# Supporting Information

**Efficient Se-rich $Sb_2Se_3$/CdS planar-heterojunction solar cells by sequential processing: control and influence of Se content**

*Pedro Vidal-Fuentes*, Marcel Placidi, Yudania Sánchez, Ignacio Becerril Romero, Jacob Andrade-Arvizu, Zacharie Jehl, Alejandro Pérez-Rodríguez, Víctor Izquierdo-Roca, and Edgardo Saucedo**

For the synthesis of Se-rich $Sb_2Se_3$ layers a sequential process is used as described in the corresponding Experimental Section. As is shown in the **Figure S1** the SLG/Mo/Sb precursors are introduced in a graphite box containing elemental Se powder, and then introduced in a tubular furnace under controlled inert atmosphere (Ar atmosphere), for the thermal annealing. The resulting absorbers are processed into solar cell devices with the substrate configuration shown in the same **Figure S1**.

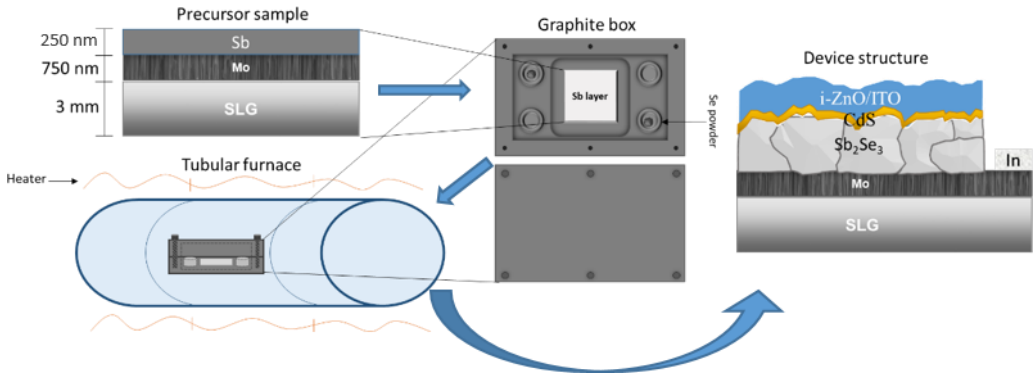


**Figure S1.** Experimental set-up followed in this work, consisting on the selenization of a metallic thermally evaporated precursor, using a graphite box in a tubular furnace.

The synthesis of $Sb_2Se_3$ layers at different total Ar pressures was investigated. As can be seen in Figure S2, for pressures below 500 mbar the layers are non-homogenous, presenting peel-off regions and making them useless as PV absorbers.

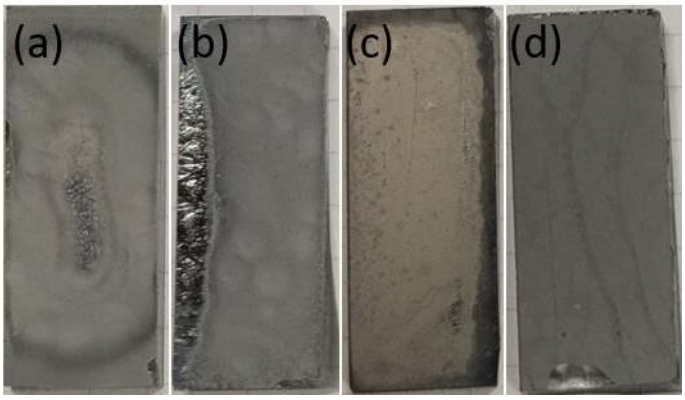


**Figure S2.** Effect of the processing pressure on the absorber morphology, selenized at a fixed temperature of 320 ºC during 30 min with 25 mg of Se at (a) 1 mbar (b) 10 mbar (c) 50 mbar (d) 500 mbar.

Figure S3 shows the IQE of selected devices fabricated with absorbers containing different 3[Sb]/2[Se] ratios together with the corresponding derivate in order to estimate the indirect and direct bandgaps. As it is clear, both of them does not depend on the composition, and values around 1.24-1.25 eV for the indirect bandgap and 1.37-1.39 eV for the direct one are obtained.

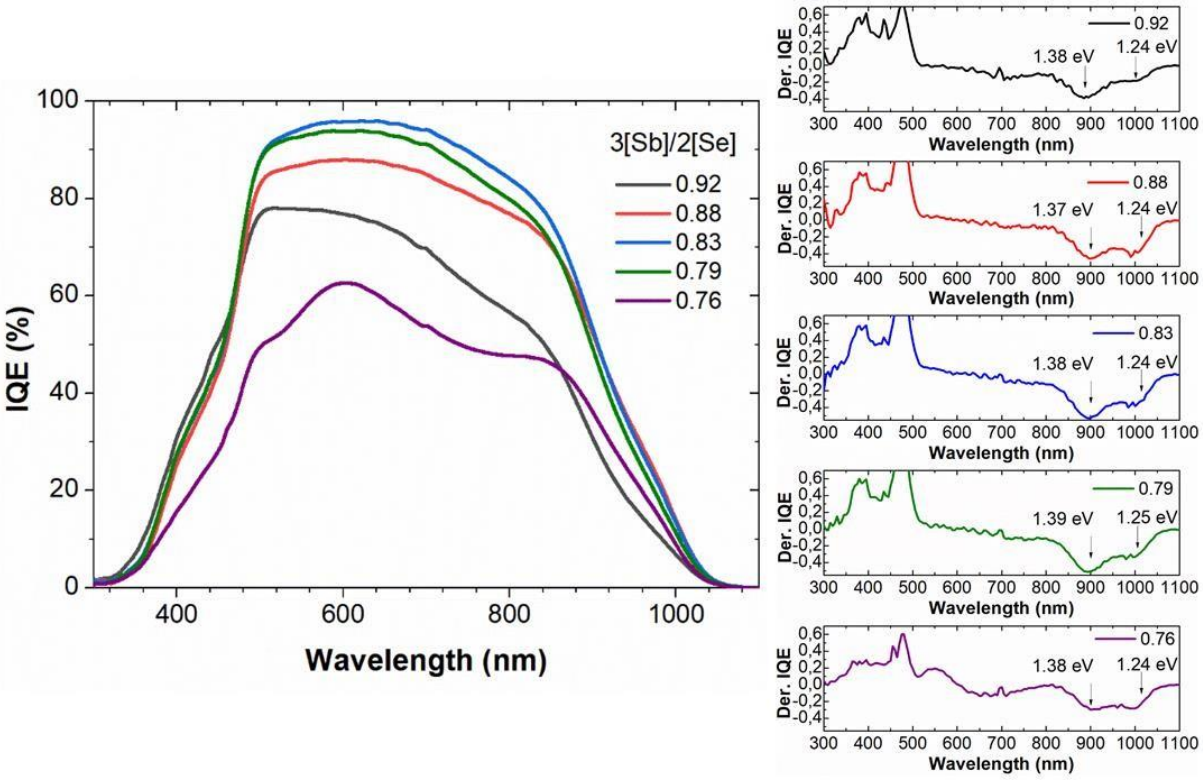


**Figure S3.** IQE of selected solar cell devices made with absorbers with different 3[Sb]/2[Se] ratios and corresponding derivate of the IQE to estimate the indirect and direct bandgaps.

Figure S4 shows the Raman spectrum in which no secondary phases aside for the orthorhombic $Sb_2Se_3$ phase. **Figure S5** shows the XRD difractogram of the champion device, demonstrating good crystalline quality, preferential [001] orientation due to a high increase in intensity of the 002 and 004 reflections, although the orientation is not uniaxial being 301 and 211 also promoted in comparison to a non-texturized samples, nevertheless this two reflections also belong to vertically aligned ribbons with some degree of tilt. [49]

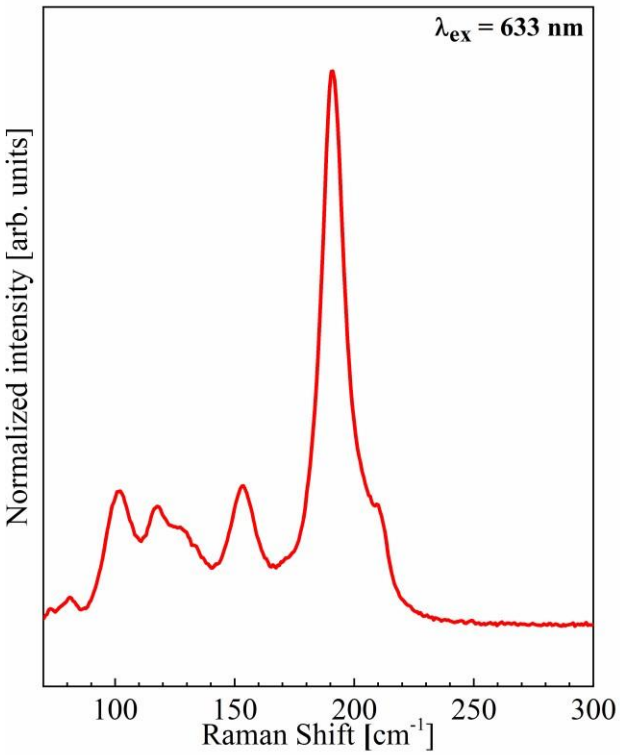


**Figure S4.** Raman spectrum of the champion solar cell

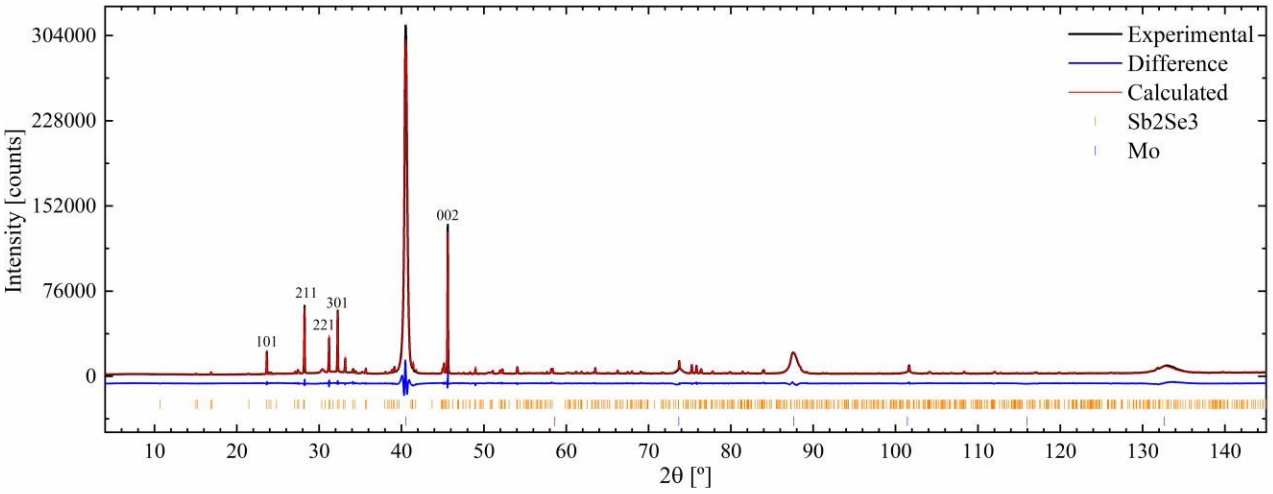


**Figure S5.** XRD difractogram and Rietveld refinement of the champion solar cell

From the linearization of **Equation 1**, that is equivalent to the y-axis on the **Figure 6**, the Urbach energy can be extracted as the inverse of the slope of the linear fit on the region E-Eg < 0; that can be understood as the characteristic energy of an exponentially decaying DOS.

$$\alpha(h\nu) = \begin{cases} A_0 \sqrt{2\exp(1)}\exp\left(\frac{h\nu - E_G}{E_U}\right) & for\ h\nu < E_G + \frac{E_U}{2} \\ A_0\sqrt{h\nu - E_G} & for\ h\nu \geq E_G + \frac{E_U}{2} \end{cases} \qquad Equation.\ S1$$